ELSEVIER

Engineering light-initiated afterglow lateral flow immunoassay for infectious disease diagnostics

Liangwen Hao [a,1], Weitao Yang [a,1], Yan Xu [a,1], Tianming Cui [a], Guoqi Zhu [a], Weiwei Zeng [a], Kexin Bian [a], Hongying Liang [a], Pengfei Zhang [b], Bingbo Zhang [a,*]

[a] *Department of Medical Ultrasound, Shanghai Tenth People's Hospital, Tongji University Cancer Center, Shanghai Frontiers Science Center of Nanocatalytic Medicine, The Institute for Biomedical Engineering and Nano Science School of Medicine, Tongji University, Shanghai, 200072, China*
[b] *Department of Central Laboratory, Shanghai Skin Disease Hospital, School of Medicine, Tongji University, Shanghai, 200443, China*

ARTICLE INFO

ABSTRACT

The pandemic of highly contagious diseases has put forward urgent requirements for high sensitivity and adaptive capacity of point-of-care testing (POCT). Herein, for the first time, we report an aggregation-induced emission (AIE) dye-energized light-initiated afterglow nanoprobes (named LiAGNPs), implemented onto a lateral flow immunoassay (LFIA) test strip, for diagnosis of two highly contagious diseases, human immunodeficiency virus (HIV) and severe acute respiratory syndrome coronavirus 2 (SARS-CoV-2) as model validation. The primary working mechanism relies on the cyclically generated singlet oxygen ($^1O_2$)-triggered time-resolved luminescent signals of LiAGNPs in which AIE dyes (TTMN) and chemiluminescent substrates (SO) are loaded. The designed LiAGNPs were found 2-fold and 32-fold sensitive than the currently used Eu(III)-based time-resolved fluorescent nanoparticles and gold nanoparticles in lateral flow immunoassay (LFIA), respectively. In addition, the extra optical behaviors of nude color and fluorescence of LiAGNPs enable the LFIA platform with the capability of the naked eye and fluorescent detection to satisfy the applications under varying scenarios. In short, the versatile LiAGNPs have great potential as a novel time-resolved reporter in enhancing detection sensitivity and application flexibility with LFIA platform for rapid but sensitive infectious disease diagnostics.

1. Introduction

The outbreak of highly contagious diseases, such as Ebola hemorrhagic fever (EBHF), dengue, coronavirus disease 2019 (COVID-19), high pathogenic avian influenza (HPAI), malaria, acquired immune deficiency syndrome (AIDS), and Middle East respiratory syndrome (MERS), has seriously threatened human health, causing global public health crises (Baker et al., 2021; Karim et al., 2020; Kirtane et al., 2021). Early and sensitive diagnosis, especially in underdeveloped areas, is one of the effective strategies to prevent the spread of pandemic infectious diseases (Ackerman et al., 2020; Miller et al., 2020; Oeschger et al., 2021; Wang et al., 2021a). The current primary diagnostic tools for infectious diseases are based on enzyme-linked immunosorbent assay (ELISA) (Grzelak et al., 2020; Li et al., 2021), reverse transcription-polymerase chain reaction (RT-PCR) (Ganguli et al., 2020; Santiago et al., 2018; Woo et al., 2020), and chemiluminescence immunoassay (CLIA) (Kyme et al., 2019; Liu et al., 2020a).

Unfortunately, these approaches are generally plagued by expensive instruments and equipment, special reagents and professional operators, and exceptionally long analysis time (Elledge et al., 2021; Ferreira et al., 2021; Yao et al., 2021; Yousefi et al., 2021). As a result, these requirements are increasingly being recognized hard to meet in barren and remote epidemic areas, even in cities when epidemics peak. Therefore, there is an urgent need to develop fast, easy operation, low-budget and portable point-of-care testing (POCT) facilities that enable patients to be conveniently and timely monitored with infectious diseases in a community or home setting (Brendish et al., 2020; Qi et al., 2021; Sebba et al., 2018).

Lateral flow immunoassay (LFIA) is currently the most commonly used POCT tool worldwide (Liu et al., 2021; Miller et al., 2020; Parolo et al., 2020; Wang et al., 2021b), of which USD 8.2 billion market size was reached in 2020. Nowadays, LFIA based on colorimetry and fluorescence as signal readout dominates the market (Hu et al., 2017a; Wang et al., 2021b; Zhang et al., 2019). Among them, colorimetric (CM)-based

LFIA, represented by gold nanoparticles (AuNPs), can quickly provide results with naked eyes. Still, it confronts a fatal shortcoming of low detection sensitivity and poor accuracy (Chen et al., 2020; Huang et al., 2019; Qin et al., 2012). In comparison, fluorescence (FL)-based LFIA is superior to CM-based LFIA in sensitivity and accuracy (Huang et al., 2020; Wang et al., 2020). However, it is being criticized for background interference. Background autofluorescence from nitrocellulose substrates, glass fibers, and biological samples are frequently found to result in incorrect readings and mislead epidemic prevention decisions (Ji et al., 2020; Liu et al., 2020b; Miller et al., 2020; Shah and Yager, 2017). Furthermore, FL-based LFIA lose the ability of visual detection by naked eyes. In resource-limited scenarios, visual detection plays an irreplaceable role. Therefore, realizing compatibility between visualization and sensitivity and promoting the versatile use of LFIA are of great practical significance.

Time-resolved fluorescence immunoassay (TRFIA) can effectively avoid the background FL by collecting the long-lived luminescence signals of the used reporters (Guo et al., 2019; Lee et al., 2020; Ma et al., 2019; Sun et al., 2021). Thanks to the low/zero background signal interference, TRFIA has a greater advantage in sensitivity than traditional FL-based LFIA. The critical component of TRFIA is the unique reporter, nowadays mainly reported from lanthanide (e.g., Eu(III)) nanoparticles. Unfortunately, the luminescence signals of lanthanide nanoparticles usually have μs ~ ms level of a lifetime (Hu et al., 2017b), and obviously, they decay too fast, thus hard to improve the detection sensitivity. Developing reporters with applicable time-resolved fluorescence emission is challenging and few materials have been reported so far.

Herein, we developed a next-generation time-resolved optical reporter, namely LiAGNPs, with a unique light-initiated afterglow phenomenon, which can sustain self-luminescence process for 20 min after removing the excitation light source due to the mild decay in luminescence (Fig. 1a). The LiAGNPs were synthesized by co-embedding two chemicals, 2-((5-(4-(diphenylamino)phenyl)thiophen-2-yl)methylene) malononitrile (TTMN), a photosensitive dye with aggregation-induced emission (AIE) characteristics (Wang et al., 2017), and N, N-dimethyl-4-(6-phenyl-2,3-dihydro-1,4-oxathiin-5-yl)aniline (SO), a chemiluminescent substrate (Jiang et al., 2019), into carboxylate-modified polystyrene nanoparticles (PSs) through a swelling method. The long-lived afterglow depends on the cascaded chemical events caused by the cyclic generation of light-triggered singlet oxygen ($^1O_2$). Leveraging this particular property of LiAGNPs as a signal transducer, we demonstrate high detection sensitivity of type 1 capsid p24 antigens (marked as p24 antigen) against Human immunodeficiency virus (HIV) and immunoglobulin M (IgM) and immunoglobulin G (IgG) against severe acute respiratory syndrome coronavirus 2 (SARS-CoV-2) on LFIA platform. In addition, the nude color (pink) and fluorescence of LiAGNPs provide two extra detection modalities for the LIFA platform, preserving naked-eye readability and enhancing its potential for use in different scenarios.

2. Experimental sections

2.1. Materials

2-((5-(4-(diphenylamino)phenyl)thiophen-2-yl)methylene)malononitrile (TTMN) dye with AIE character was synthesized according to the previous protocol of our laboratory without any change (Wang et al., 2017). (N, N-dimethyl-4-(6-phenyl-2,3-dihydro-1,4-oxathiin-5-yl)aniline) (SO) was purchased from Shanghai Yaxing Biomedical Technology Co., LTD (Shanghai, China). Carboxylate-modified polystyrene nanoparticles (PSs) were purchased from So-Fe Biomedicine (Shanghai, China). N-(3-(dimethylamino)propyl)-N′-ethylcarbodiimide hydrochloride (EDC), 1-methoxy-2-propanol, sucrose, Tween-20, Bovine serum albumin (BSA), H$_2$O$_2$, sodium molybdate, sodium chloride, chloroauric acid, trisodium citrate, and sodium borate were purchased from Aladdin

Industrial Inc. Singlet oxygen sensor green (SOSG) were purchased from Beyotime Biotechnology. The carboxylic Eu(III)-based time-resolved fluorescent nanoparticles (Eu-TRFN) with size of 190 nm were purchased from taoyugroup.com (Shanghai, China). Sample pads, conjugate pads, absorbent pads, NC membrane, PVC backing pad, and plastic shell were purchased from Shanghai Kinbio Biotechnology Co., Ltd (Shanghai, China). Anti-p24 antigen detection monoclonal antibodies (mAb1), anti-p24 antigen capture monoclonal antibodies (mAb2), and p24 antigens were purchased from Cnpair Biotechnology Co., Ltd (Hangzhou, China). Goat anti-mouse IgG, goat anti-chicken IgY, influenza A protein (IFA), influenza B protein (IFB), C-reactive protein (CRP), procalcitonin (PCT), and human chorionic gonadotropin (HCG) were purchased from Nanjing Santa Scott Biotechnology Co., Ltd (Nanjing, China). SARS-CoV-2 IgG, IgM, S-antigen, mouse anti-human IgM, and mouse anti-human IgG were purchased from Fapon Biotechnology Co., Ltd (Guangzhou, China). The ELISA kit for p24 antigen detection was purchased from Abmart Biomedicine (Shanghai) Co., LTD (Shanghai, China). Deionized water was provided by a Milli-Q purification system. All serum samples were collected from healthy volunteers with signed informed consent. All experiments involved the use of healthy human serum samples were approved by the Drug Trial Ethics Committee of Shanghai Skin Disease Hospital.

2.2. Instrument and characterization

Hitachi HT7700 Exalens transmission electron microscope (Hitachi Co., Ltd., Japan) was employed to provide TEM images at 200 kV. Hydrodynamic diameter distribution and zeta-potential were acquired on a dynamic light scattering analyzer (Malvern Zetasizer Nano ZS). The UV–vis absorption spectra were recorded by Genesys 10s UV–vis spectrophotometer (Thermo Scientific, Waltham, MA). Fluorescence spectra were obtained using a Hitachi F-7000 fluorescence spectrophotometer. Afterglow images and intensity were collected by a darkroom CCD camera. Time-resolved strip analyzer, fluorescent strip analyzer, and colloidal gold strip analyzer were purchased from Hangzhou Autokun Tech (Hangzhou, China).

2.3. Synthesis of LiAGNPs

LiAGNPs were synthesized via the means of the swelling method. In brief, 5 mg of TTMN and 3 mg of SO were mixed and dissolved in 3 ml of 1-methoxy-2-propanol (PGME) solution, and preheated to 70 °C. Subsequently, 1 mL of PSs (100 mg mL^{-1}) were added and reacted for 30 min. Then immediately stop heating and cool the solution to room temperature. The synthesized LiAGNPs were washed three times with deionized water, centrifuged at 13500 rpm for 15 min, and the residue was re-dispersed in 4 mL of deionized water. The as-prepared LiAGNPs solution was stored in the dark at 4 °C for future use. The TNPs (only doped 5 mg of TTMN) and SNPs (only doped 5 mg of SO) were synthesized using the same swelling protocols.

2.4. Afterglow emission measurement

Afterglow images were collected using a darkroom CCD camera. In brief, 20 μL of LiAGNPs (20 mg mL^{-1}) was added to Eppendorf (EP) tubes containing 180 μL of deionized water, and then pre-illuminated with a white LED flashlight (2000 lm) for 1 min. The afterglow images were acquired employing an open filter (full-wave reception), and the afterglow emission decay process was obtained continuously by the CCD camera without any traveling of the sample. The Andor SOLIS software was employed to analyze the afterglow images. For investigating whether the afterglow emission involved $^1O_2$ or not, 20 μL LiAGNPs (20 mg mL^{-1}) were incubated with 90 μL Na$_2$MoO$_4$ (10 mM) and 90 μL H$_2$O$_2$ (4 mM) for 5 s, before afterglow images were collected.
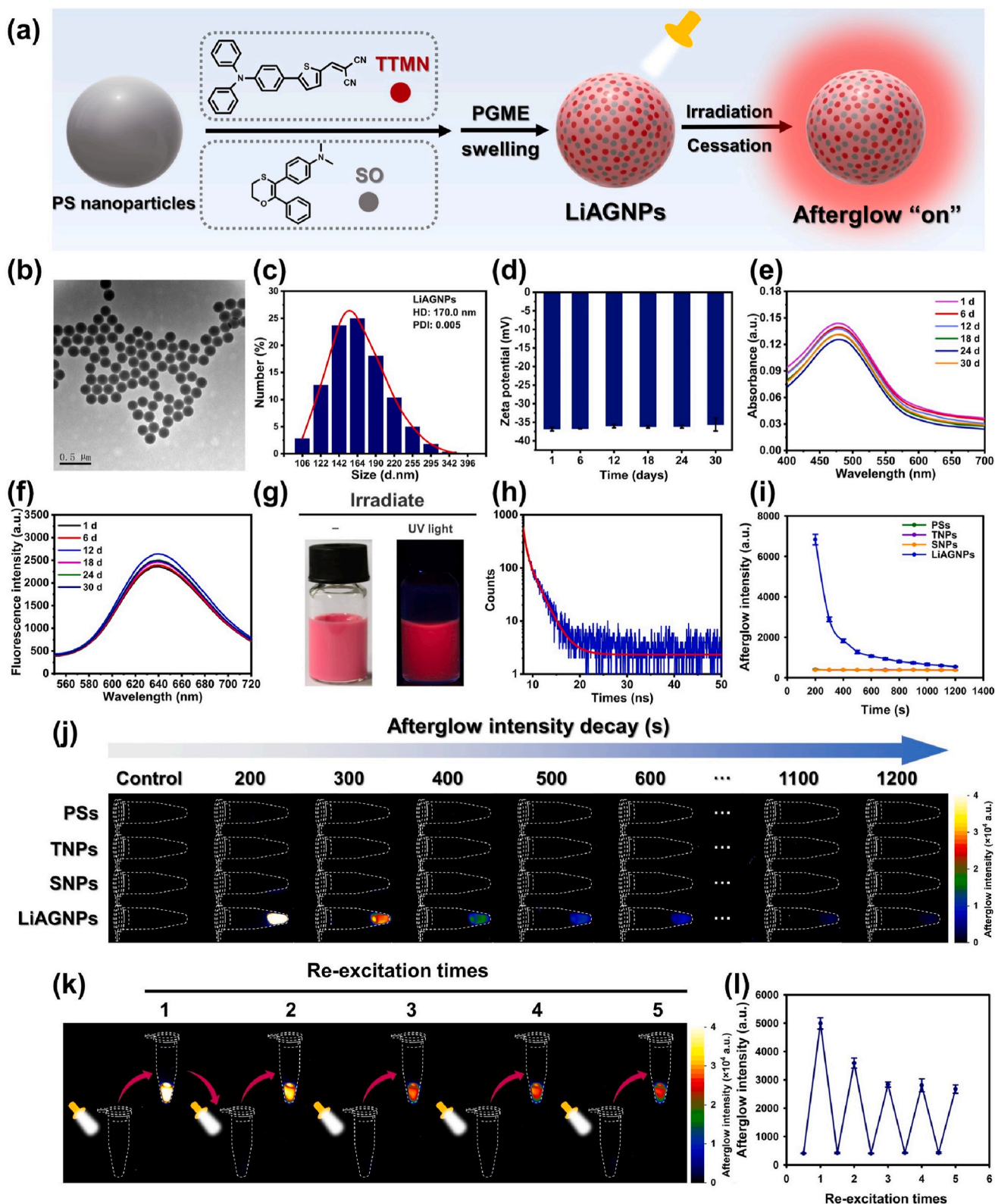
Fig. 1. Synthesis and characterizations of LiAGNPs. (a) Schematic diagram of the synthesis of LiAGNPs using the swelling method. (b) TEM image of LiAGNPs. Scale bars, 0.5 μm. (c) HD distribution and of LiAGNPs in water. (d–f) Zeta potential (d), UV–vis absorption spectrum (e), and fluorescence spectra (f) of LiAGNPs against long-term storage for 30 days. (g) The digital photo of LiAGNPs under room light (left) and UV light (right). (h) The fluorescence lifetime of LiAGNPs. (i–j) The quantitative decay intensity (i) and dynamic afterglow decay images (j) of PSs, TNPs, SNPs, and LiAGNPs (2 mg mL^{-1}) were acquired after 1 min exposure to a white LED lamp (2000 lm) using a dark room CCD camera. No white LED lamp irradiation as a control. (k–l) The afterglow emission images (k) and their quantitative intensity values (l) of LiAGNPs were re-excited with the same LED lamp for 1 min. The error bars were obtained from three parallel experiments.

2.5. Evaluation of $^1O_2$ generation

SOSG (50 μM) with a volume of 100 μL was placed in LiAGNPs solution (0.1 mg mL^{-1}, 2 mL), and exposed to a white LED flashlight (2000 lm) lasts 1 min. Then, a Hitachi F-7000 fluorescence spectrophotometer was employed to recorded the fluorescence spectrum of SOSG solution (504 nm for excitation, 525 nm for emission).

2.6. Synthesis of LiAGNPs–mAb1

The LiAGNPs–mAb1conjugates were prepared via the EDC-mediated covalent attachment of LiAGNPs and mAb1. In short, the as-synthesized LiAGNPs (20 mg mL^{-1}) with a volume of 5 μL, mAb1 (10 μg), and EDC (5 μg) were mixed in 200 μL PBS solution (0.01 M, pH 7.0), and the mixed solution was gently stirred 30 min (room temperature). Then, BSA solution (100 μL, 10% w/v) and EDC (10 μg) were placed for 1 h under continuous gently stirring. Finally, the reaction-completed solution was centrifuged at 15000 rpm for 15 min and the precipitate was redispersed in PBS solution (0.01 M, pH 7.4) with a volume of 50 μL, containing 25% sucrose (w/v), 1% BSA (w/v), 1% Tween-20 (v/v), and 0.1% sodium nitride (NaN$_3$, w/v). The prepared LiAGNPs–mAb1 conjugates were placed at 4.0 °C for use. The synthetic process of Eu–TRFNs–mAb1 is the same as LiAGNPs–mAb1.

2.7. Synthesis of AuNPs–mAb1

The AuNPs with size of 20 nm were synthesized according to the previous report without any change (Li et al., 2016). The AuNPs–mAb1 immunoprobes were synthesized via electrostatic adsorption. Typically, 10 μg of mAb1 was added to 1.0 mL of AuNPs solution. The mixed solution was gently stirred for 30 min of incubation at room temperature. Then, 10% BSA (w/v) with a volume of 100 μL was added another for 1 h of incubation under continuous gently stirring. Finally, the reaction-completed mixed solution was purified through centrifugation at 15000 rpm for 15 min and redispersed in PBS solution (0.01 M, pH 7.4) with a volume of 200 μL, involving 25% sucrose (w/v), 1% BSA (w/v), 1% Tween-20 (v/v), and 0.1% sodium nitride (NaN$_3$, w/v). The prepared AuNPs–mAb1 conjugates were placed at 4.0 °C for future use.

2.8. Fabrication of LiAGNPs–LFIA test strip for p24 antigen assay

The LiAGNPs–LFIA strip for p24 antigen detection was fabricated referring to the previous literature (Hao et al., 2020). Firstly, mAb2 (2.0 mg mL^{-1}) and goat anti-mouse IgG (2.0 mg mL^{-1}) pre-dispersed in PBS solution (pH 6.0, containing 5% w/v sucrose, 0.2% w/v BSA, and 1% v/v NaCl) were deployed to the NC membrane as the T- and C-line, respectively. Subsequently, the spraying finished NC membrane was dried overnight in a 37 °C incubator. The prepared LiAGNPs–mAb1 were dried on the conjugate pad overnight at 37 °C with a dose of 3.0 μL in each strip. The sample pads were pretreated with sodium borate buffer (20 mM, pH 8.0, containing 1.0% w/v BSA, 0.25% v/v Tween-20, and 0.1% w/v NaN$_3$), and the placed in a 37 °C incubator to dry overnight. Finally, the processed NC membrane, conjugate pads, and sample pads were fitted into a PVC backing pad, and the back pad was cut into 3.8 mm wide and mounted in a plastic shell for standby. TRFN–LFIA and AuNPs–LFIA test strips are prepared in the same way as LiAGNPs–LFIA strip.

2.9. Assay procedure of LiAGNPs–LFIA test strip for p24 antigen in human serum

In a typical detection process, 70 μL of the sample was injected into the sample sink. After a 15 min incubation, the signal answers (containing CM, FL, and afterglow) of the T- and C-line were collected by the naked eye, handheld UV flashlight, or corresponding strip analyzer. The detection process of Eu–LFIA and AuNPs–LFIA test strips are the same as

LiAGNPs–LFIA strip.

2.10. Synthesis of LiAGNPs–S-antigen and LiAGNPs–Chicken IgY

The synthetic process of LiAGNPs–S-antigen were similar to LiAGNPs–mAb1 with some modifications. In short, the as-synthesized LiAGNPs (20 mg mL^{-1}) with a volume of 5 μL, S-antigen (5 μg), and EDC (5 μg) were mixed in 200 μL PBS solution (0.01 M, pH 8.0), and followed by gently stirred for 30 min incubation (room temperature). Subsequently, 10% BSA (w/v) solution with a volume of 100 μL and EDC (10 μg) were injected for 1 h under continuous gently stirring. The following synthetic process is the same as LiAGNPs–mAb1.

The preparation process of LiAGNPs–Chicken IgY is the same as that of LiAGNPs–S-antigen, and it is only necessary to replace S-antigen with Chicken IgY.

2.11. Fabrication of LiAGNPs–LFIA strip for SARS-CoV-2 IgM and IgG assay

The fabrication procedure of LiAGNPs–LFIA strip for SARS-CoV-2 IgM and IgG assay was similar to p24 antigen test strip with some modifications. Briefly, 3.0 mg mL^{-1} of anti-human IgM, 3.0 mg mL^{-1} of anti-human IgG, and 1.0 mg mL^{-1} of goat anti-chicken IgY were pre-dispersed in PBS solution (0.01 M, pH 6.0, including 5% sucrose (w/v), 0.2% BSA (w/v), and 1% NaCl (v/v) were deployed to the NC membrane as the M-line, G-line, and C-line, respectively. Afterward, the spraying finished NC membrane was placed in a 37 °C incubator to dry overnight, immediately. The prepared LiAGNPs–S-antigen and LiAGNPs–chicken IgY immunoprobes were dried on the conjugate pad overnight at 37 °C with a dose of 4.0 μL in each strip. The following process is the same as LiAGNPs–LFIA test strip for p24 antigen assay.

2.12. Assay procedure of SARS-CoV-2 IgM and IgG in FBS using LiAGNPs–LFIA test strip

In a typical detection process, 70 μL of mixed FBS samples containing a series of IgG and IgM was injected into the sample sink. After incubation for 15 min, the signal answers (including CM, FL, and afterglow) of the M-, G-, and C-line were collected by the naked eye, handheld UV flashlight or corresponding strip analyzer.

3. Results and discussion

3.1. Synthesis and characterization of LiAGNPs

TTMN dye and SO molecules, which are two core elements, were used as functional building blocks to synthesize LiAGNPs with afterglow property, as demonstrated in Fig. 1a. In a typical process, TTMN and SO were co-encapsulated into carboxylate-modified PSs in 1-methoxy-2-propanol (PGME) utilizing the swelling method. The large-area transmission electron microscope (TEM) image in Fig. 1b displays good spherical morphology and dispersion of the resulting LiAGNPs, which is similar to the untreated PSs (Fig. S1). The hydrodynamic diameter (HD) of LiAGNPs (170.0 nm, Fig. 1c) was found pretty similar to that of the original PSs (Figs. S1 and S2). Zeta potential analysis exhibited that the surface charge of LiAGNPs was negative (−36.9 mV, Fig. 1d), facilitating the monodisperse of LiAGNPs in solution. UV–Vis and fluorescence spectra of the synthesized LiAGNPs in Fig. 1e and f show that the absorption maximum and the emission maximum of the LiAGNPs are 482 nm and 640 nm, respectively. The photographs in Fig. 1g exhibit that the solution color of LiAGNPs is pink, which is easy for human eyes to recognize. Meanwhile, it can be found to emit red FL under the excitation of ultraviolet (UV) light. The average FL lifetime of LiAGNPs was found at the nanosecond level, showing the characteristics of instantaneous luminescence (Fig. 1h). We speculated that this FL property is derived from the TTMN dye inside LiAGNPs. Moreover, by measuring

the UV absorption spectrum, the actual contents of TTMN and SO were determined to be 4.0 μg mg^{-1} and 0.36 μg mg^{-1} of PSs, respectively (Fig. S3). These findings indicate that the prepared LiAGNPs not only could serve as a CM label to achieve the signal output strategy by naked eye acquisition, but also be used as a FL label under external light excitation.

Besides the above optical performance and, more importantly, the engineered LiAGNPs were found to have long-live light-initiated afterglow luminescence. To better describe this property, two control nanospheres of similar particle sizes to LiAGNPs, including TNPs (only using TTMN as active molecules) and SNPs (only using SO as active molecules), were prepared via the same swelling protocols and further confirmed by TEM and DLS analysis (Fig. S4). As shown in Fig. 1i and j, the dynamic afterglow intensity and images of LiAGNPs display persistent luminescence for 20 min post 1 min of irradiation by a white LED lamp (2000 lm). By contrast, none of the PSs, TNPs, and SNPs exhibit signals after ceasing irradiation. This excellent time-gated luminescence property is very beneficial improving detection sensitivity for the LFIA platform. Interestingly, the re-excited afterglow signals of LiAGNPs were found to still maintained more than half of the initial intensity even after five rounds of irradiation, demonstrating their repeatable acquisition ability if necessary (Fig. 1k and l). We further investigated the effects of light initiation time and the afterglow signal collection time on afterglow intensity. As shown in Fig. S5, when the afterglow signal collection time (100 s, Fig. S5a) or light initiation time (60 s, Fig. S5b) was fixed, we found that the afterglow intensity of LiAGNPs was positively related to the initiation time and the signal collection time. It is worth pointing out that when the light initiation time exceeds 60 s, the intensity of

afterglow collected was found decreased (Fig. S5a). This could be attributed to the synchronous engergy release of LiAGNPs while irradiated by LED light. Other further characterizations including Zeta potential (Fig. 1d), UV–vis absorption spectrum (Fig. 1e), fluorescence spectrum (Fig. 1f), afterglow intensity (Fig. S6), and HD (Fig. S7) of LiAGNPs show that no significant changes were observed after 30-day storage, indicating the superb colloid stability and no leakage or deterioration phenomenon in long-term storage. These high colloidal and optical stability are attributed to the polystyrene matrix which completely isolates the internal dyes from the external environment.

3.2. Light-initiated afterglow mechanism study of LiAGNPs

AIE dye TTMN used in this work has been proved to be a powerful photosensitizer with high $^1O_2$ production (Wang et al., 2017; Zhang et al., 2021b). Specifically, the electron of photosensitizers transition from the ground state to the triplet excited state under the irradiation of the external light source through itersystem crossing (ISC). The energy of the triplet excited photosensitizers are then transferred to molecular oxygen to form $^1O_2$ (Lucky et al., 2015; Shi et al., 2020). In this study, we designed LiAGNPs by simultaneously embedding photosensitive AIE dye TTMN and chemiluminescent molecule SO, aiming to produce afterglow luminescence via $^1O_2$ as an energy transfer channel. First, singlet oxygen sensor green (SOSG), a $^1O_2$ indicator, was applied to verify the $^1O_2$ generation of LiAGNPs and it demonstrates increasing $^1O_2$ generation with a white LED light irradiation (Fig. 2a and b). At the same time, there was no remarkable $^1O_2$ generation in the sample of SNPs or PSs. These results clearly reveal that TTMN can produce $^1O_2$ efficiently under
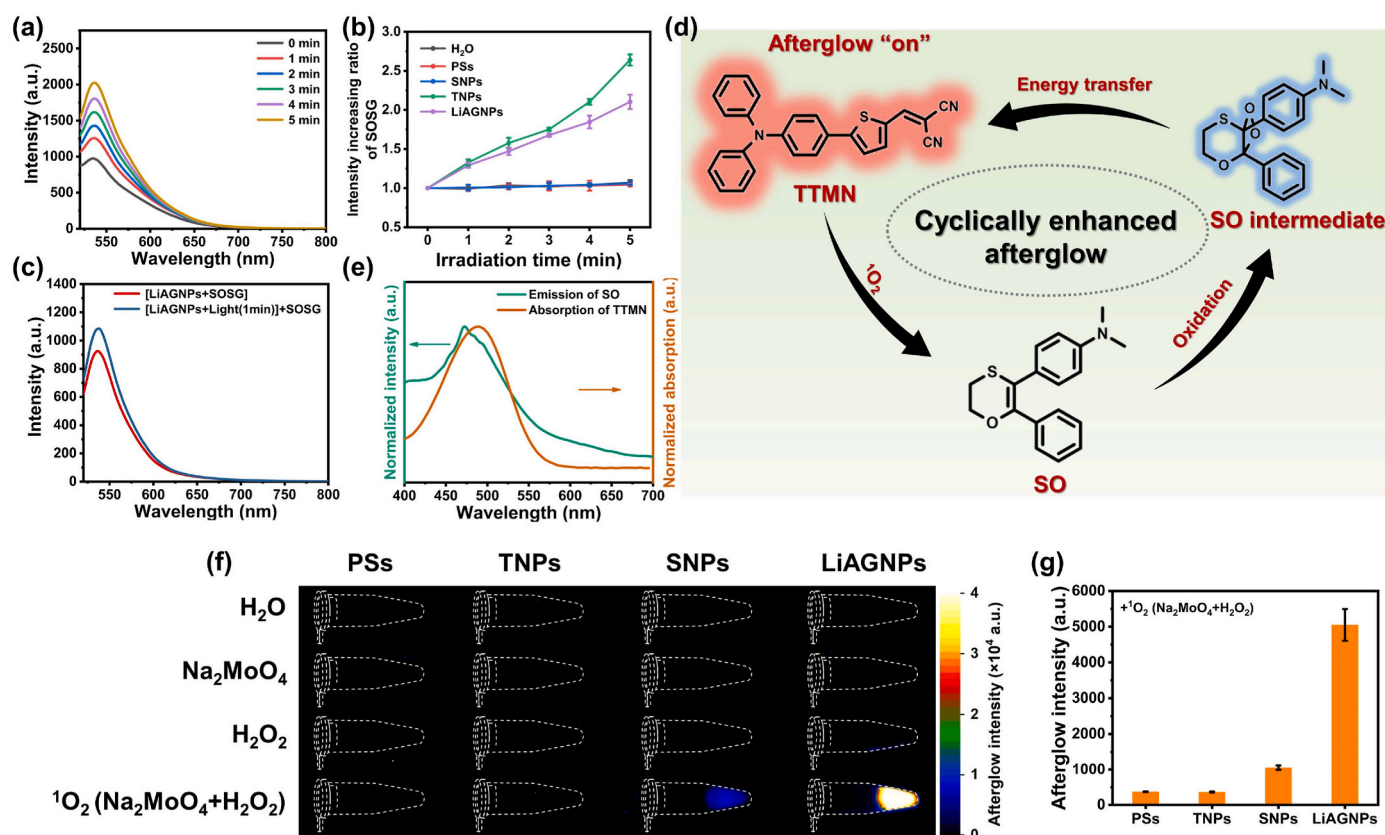

Fig. 2. Afterglow mechanism study. (a–b) Fluorescence spectra (a) and normalized fluorescence intensity increasing ratio (b) of SOSG, with final concentration at 2.5 μM in LiAGNPs (0.1 mg mL^{-1}) solution, were recorded every 1 min for 5 min upon exposed to a white light lamp (2000 lm). (c) Fluorescence spectrum of SOSG (2.5 μM, final concentration) in LiAGNPs (0.1 mg mL^{-1}) solution, in which SOSG was added after pre-irradiating LiAGNPs solution with white light lamp (2000 lm) for 1min. (d) Schematic illustration of afterglow mechanism of LiAGNPs. (e) The absorption spectrum of TTMN dyes and the fluorescent emission spectrum of SO molecule after normalization. (f–g) Afterglow luminescence images (f) and intensity (g) of PSs, TNPs, SNPs, and LiAGNPs (2 mg mL^{-1}, final concentration) incubated with H_2O, Na_2MoO_4, H_2O_2, or $Na_2MoO_4 + H_2O_2$ for 5 s, respectively. The error bars were obtained from three parallel experiments.

light, and SO molecule cannot have the ability to produce $^1O_2$. Of interest, we noticed that TNPs provide more $^1O_2$ than LiAGNPs (Fig. 2b). This is most likely due to $^1O_2$ consumption by the SO molecule in the LiAGNPs sample. Because $^1O_2$ produced by TTMN can react with SO to form an intermediate, the determined amount of $^1O_2$ in LiAGNPs decreases.

To further investigate the $^1O_2$ channel in LiAGNPs, then, a process of pre-treating LiAGNPs and TNPs samples with white LED light (2000 lm, 1 min) irradiation was operated, followed by the addition of SOSG $^1O_2$ indicator. It can be seen that the FL intensity of SOSG in the LiAGNPs sample is significantly enhanced compared with that without light pre-irradiation (Fig. 2c). However, there is no enhancement in SOSG FL intensity in the example of TNPs + light irradiation (Fig. S8). This increased FL intensity in the example of LiAGNPs clearly shows increased $^1O_2$ production in LiAGNPs. It should be stated that the survival time of $^1O_2$ in aqueous is less than 10 μs, so the pre-irradiation–induced $^1O_2$ vanished before the followed measurement. Thus, this increased $^1O_2$ production is not directly due to the pre-irradiation by LED but to the newly generated $^1O_2$. Based on the above evidence and the results from the control experiments on TNPs, it can be concluded that pre-irradiation produces $^1O_2$ and $^1O_2$ can be newly and circularly generated in LiAGNPs after removing the LED light sources. The working mechanism is proposed in Fig. 2d. This specific design, and the big spectral crossover between the absorption spectrum (400 nm–600 nm) of TTMN dye and the emission spectrum (450 nm–650 nm) of SO dye (Fig. 2e), favor energy transfer between these two dyes to form afterglow.

In addition to white LED light irradiation, we used the H_2O_2-molybdic acid (e.g., Na_2MoO_4) system, a standard system that produces $^1O_2$, to test the afterglow performance of LiAGNPs. It should be noticed that SO is a chemiluminescent substrate that can react with $^1O_2$ to produce chemiluminescence (Jiang et al., 2019). As shown in Fig. 2f and g, LiAGNPs show a much higher luminescence, while PSs and TNPs remain unlit after being treated with Na_2MoO_4 + H_2O_2. These results confirm that LiAGNPs hold good afterglow performance, and can be initiated by Na_2MoO_4 + H_2O_2. Interestingly, the afterglow intensity of LiAGNPs excited by Na_2MoO_4 + H_2O_2 was found significantly higher than that of SNPs (≈5.0-fold). From the above results, it can be collectively concluded that the afterglow property of LiAGNPs is mainly due to a $^1O_2$ cyclic generation mechanism (Fig. 2d). To be specific, TTMN dye, as a photosensitizer in LiAGNPs, firstly generates sufficient $^1O_2$ after white LED light irradiation. Subsequently, the SO molecule, as the chemiluminescence substrate in LiAGNPs, is attacked by $^1O_2$ to form a high-energy but unstable SO-dioxetane intermediate, fluently transferring energy to the TTMN dye to emit photons and further implement the next round of $^1O_2$ and afterglow generation.

3.3. Principle of LiAGNPs based LFIA

A closed-loop of "photon-$^1O_2$-photon" afterglow emission was testified in our work that provides much longer afterglow emission (≈20 min) even after the cessation of the excitation light which favors for signal collection. Encouraged by this unique time-gated light-initiated afterglow as well as the extra FL and nude color tri-optical behavior of LiAGNPs, the practicable of employing LiAGNPs as a novel reporter was studied on the LFIA platform (LiAGNPs–LFIA) for POCT of infectious diseases. Although persistent luminescence nanoparticles in the LIFA detection have been developed (Paterson et al., 2014; Zhang et al., 2021a), they are generally prepared at very high temperature via a sintering method which make them hard dispersed in aqueous phase. Actually, in our group, we did synthesize such persistent luminescence inorganic nanoparticles and it took us a lot of efforts to modify its surface for bioimaging (Wang et al., 2018). By contrast, the LiAGNPs proposed in this work exhibit good water dispersibility and ease of synthesis which is conducive to coupling with antibodies and the following bioassay.

p24 antigen, the earliest protein biomarker in HIV-infected patients (Gray et al., 2018; Pandori et al., 2009), was employed as examples to demonstrate the detection performance of LiAGNPs. The carboxylated LiAGNPs were modified with anti-p24 detection monoclonal antibodies (mAb1) through 1-ethyl-3-(3-dimethylaminopropyl) carbodiimide (EDC)-introduced covalent attachment (Chen et al., 2022; Norman et al., 2020) to constitute LiAGNPs–mAb1 as detection probes (Fig. S9). Increased HD and changed zeta-potential of LiAGNPs–mAb1 indicate mAb1 was successfully modified onto the surface of LiAGNPs to form LiAGNPs–mAb1 immunoprobes (Figs. S10a and S10b). The mechanism of the designed LiAGNPs–LFIA test strip for point-of-care HIV p24 antigen detection is presented in Fig. 3a. The LFIA test strip was established by deploying anti-p24 capture monoclonal antibodies (mAb2) and goat anti-mouse IgG on the nitrocellulose (NC) membrane as the T- and C-line, respectively. For HIV-infected sample assay, the p24 antigen is first captured by LiAGNPs–mAb1 detection probes (pre-deposited on the conjugate pad) and then arrested by mAb2 fixed, forming a sandwich immunocomplex on the T-line as a detection signal. The remaining detection probes are combined with goat anti-mouse IgG appointed as a quality control signal on the C-line. In contrast, in the case of a negative test, no immunocomplex is formed, and thus, no LiAGNPs nanocomposites can be collected in the T-line.

Based on the tri-functions of LiAGNPs, the proposed LiAGNPs–LFIA has triple signal output modalities (i.e., afterglow, FL, and CM). In detail, the CM modality allows evident pink bands on the T-line and C-line for rapid visual qualitative testing without specific equipment and operation or quantitatively determined by a commercial colloidal gold strip analyzer. The FL modality can be visual qualitatively under an extra handheld ultraviolet (UV) lamp or quantitatively determined by a fluorescent strip analyzer. More importantly, the afterglow modality further enables higher signal-to-background ratio (SBR), sensitive and accurate quantification of p24 antigen by using commercially available time-resolved strip analyzer (white LED light irradiation for 100 μs, pause for 50 μs, and afterglow signal collection for 400 μs) to avoid false positive/negative results (Fig. 3b). The test results demonstrate for the analysis of p24 antigen employing the LiAGNPs–LFIA is displayed in Fig. 3b. Notably, if the band of the C-line is absent, the detection result is invalid.

3.4. Parameter optimization of LiAGNPs–LFIA

To obtain optimal sensitivity and appropriate signal intensity from the T- and C-lines, several vital parameters (including the labeling amount of mAb1, the mAb2 sprayed on the T line, the used volume of LiAGNPs–mAb1 immunoprobes in each test strip, and the reaction time for signal acquirement) in the development process of LiAGNPs–LFIA were systematically optimized. All parameter optimization processes were conducted by detecting p24 antigen spiked HIV-free human serum sample (3.0 ng mL^{-1}), and the test was repeated three times for each sample. The optimal parameters were confirmed relied on the acquired highest T/C (the ratio of signal intensity on the T-line to that on the C-line), including CMI_T/CMI_C value (the ratio of colorimetric intensity), FLI_T/FLI_C value (the ratio of fluorescent intensity), and AGI_T/AGI_C value (the ratio of afterglow intensity).

Fig. S11 display that insufficient amount of labeled mAb1 will affect the antigen capture efficiency. At the same time, excessive antibodies may produce spatial hindrance on the surface of LiAGNPs and shield its active site, lowering the T-line signal intensity. Therefore, the optimal labeling amount of the antibody was determined to be 100 μg mg^{-1} of LiAGNPs. As shown in Fig. S12, all T/C signal ratios of the LiAGNPs–LFIA test strip gradually reach a plateau as the concentration of mAb2 fixed on the T-line increases to 2.0 mg mL^{-1}, demonstrating that the optimal concentration of mAb2 is 2.0 mg mL^{-1}. Varying volume amounts of LiAGNPs–mAb1 immunoprobes in each test strip were further operated, the highest T/C value was found at a dosage of 3.0 μL (Fig. S13). To determine the optimal reading time for LiAGNPs–LFIA test
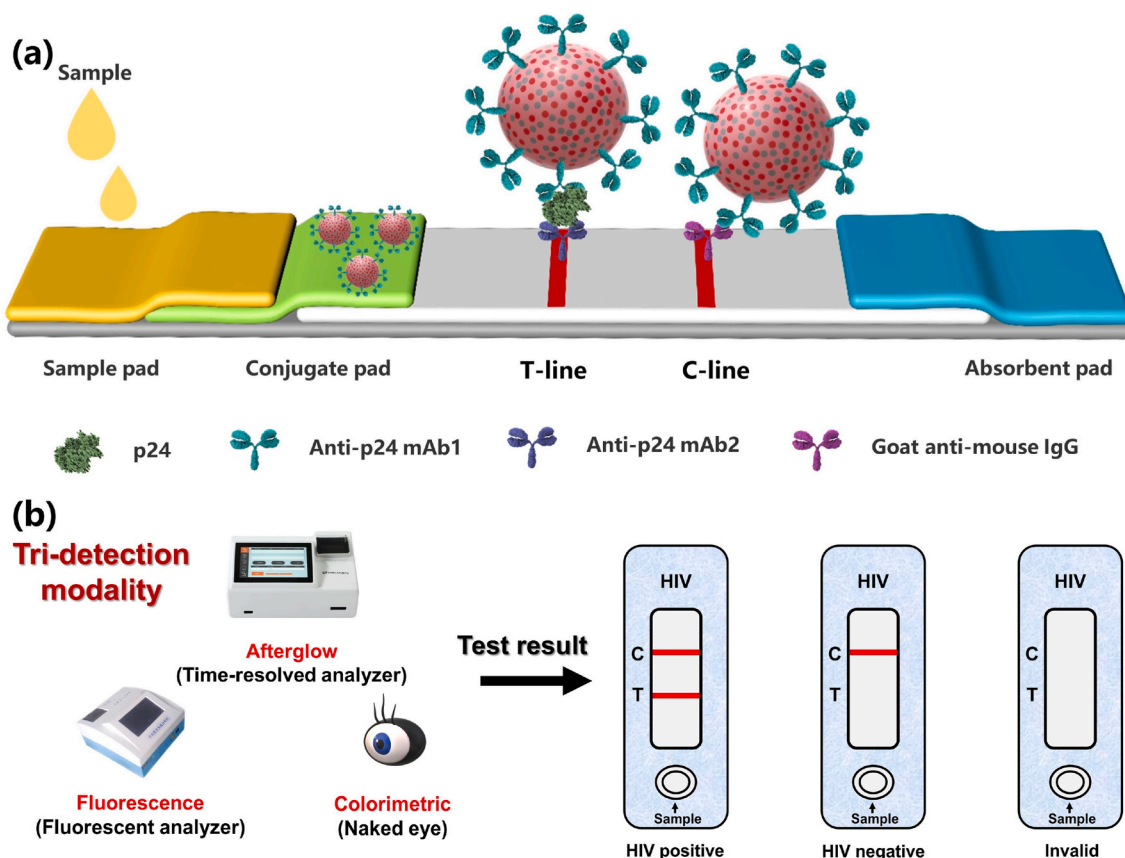
Fig. 3. Working mechanism schematic of LiAGNPs–LFIA test strip platform. (a) Schematic representation for p24 antigen detection using LiAGNPs–LFIA test strip platform. (b) Detection modality and interpretation of different detection results. The presence of a signal band on both the T-line and C-line shows HIV positivity; only the company of a signal band on C-line represents HIV negativity; none of the signal bands on the T-line and the C-line represent an invalid test result.

strip, the immunoreaction kinetics curve was plotted by measuring the T/C values at different counter times. As shown in Fig. S14, most of the T/C values achieve a balance after 15 min, which indicates that 15 min for immunoreaction in the LiAGNPs–LFIA step is sufficient for credible p24 antigen assay.

3.5. Analytical evaluation of LiAGNPs–LFIA for p24 antigen

For comparison, the commercial Eu(III)-based time-resolved fluorescent nanoparticles (Eu-TRFNs) with similar size of 190 nm was introduced on LFIA (named Eu–LFIA). Since both LiAGNPs and Eu-TRFNs were based on PSs with similar particle size, the preparation parameters of Eu–LFIA were consistent with those of LiAGNPs–LFIA. Two commercially available time-resolved strip analyzers with slightly different parameters (for LiAGNPs–LFIA: 470 nm white LED light irradiation 100 μs, pause 50 μs, and 640 nm afterglow emission signal collection 400 μs; for Eu–LFIA: 365 nm UV light irradiation 100 μs, pause 50 μs, and 615 nm fluorescent emission signal collection 400 μs) were employed for quantitative assay of p24 antigen. The limit of detection (LOD) was defined as the lowest p24 antigen concentration corresponding to SBR >1. The SBR is the ratio of the T/C value of the p24 antigen positive serum sample to the background values, which is defined as the average of the T/C values from 20 p24 antigen-negative serum samples plus a threefold standard deviation.

Under the optimized parameters, LiAGNPs-LFIA and Eu-LFIA were employed to detect human serum sample solutions with different concentrations of p24 antigen in the range of 0–100 ng mL^{-1}. As shown in Fig. 4a, the LOD for p24 antigen detection of the proposed LiAGNPs–LFIA was 0.006 ng mL^{-1}, which is 2-fold lower than that by Eu–LFIA (0.012 ng mL^{-1}). The lower LOD of the LiAGNPs–LFIA test

may be due to the unique light-initiated afterglow characteristics of LiAGNPs, in which luminescence mildly decays after ceasing light excitation. It is worth noting that increasing emission signal collection time of the strip analyzer theoretically can further increase the detection sensitivity of LiAGNPs–LFIA. There are two main reasons. First, the light-initiated luminescence of LiAGNPs can be maintained for 20 min (Fig. 1i and j), while Eu chelates only last microseconds to milliseconds. Second, the higher afterglow intensity can be obtained by appropriately increasing the light initiation time and afterglow signal collection time of the analyzer (Fig. S5), which may lead to the increased sensitivity of LiAGNPs–LFIA. And importantly, we found that these LiAGNPs can be successfully applied to high-contrast and time-resolved afterglow detection without using a sophisticated time-shutter device. A good correlation curve between the concentration of p24 antigen and T/C ratio was obtained in LiAGNPs–LFIA and Eu–LFIA strips for p24 antigen quantitation (Fig. 4b). The corresponding equation are as follows: y = 0.1505x$^{0.8713}$ (R^2 = 0.9975) (LiAGNPs–LFIA) and y = 0.1131x$^{0.9615}$ (R^2 = 0.9973) (Eu–LFIA).

It should be pointed out that the color of commercial Eu-TRFN is white, while the color of LiAGNPs proposed by this work is pink (Fig. 1g). Therefore, LiAGNPs provide a complementary CM modality to qualitative diagnosis for p24 antigen using naked-eye without instruments under some special scenarios. Meanwhile, LiAGNPs also have FL property provided by the internal TTMN dye, which enables visualization under a handheld flashlight (365 nm UV light) and quantification using a fluorescence strip analyzer. To evaluate the CM and FL modality detection performance of LiAGNPs, 20 nm AuNPs based–LFIA (AuNPs–LFIA), the most popular POCT device, was established as a control demonstration. The detailed optimization process of AuNPs–LFIA are shown in Fig. S15. As shown in Fig. 4c, the LOD for p24 antigen
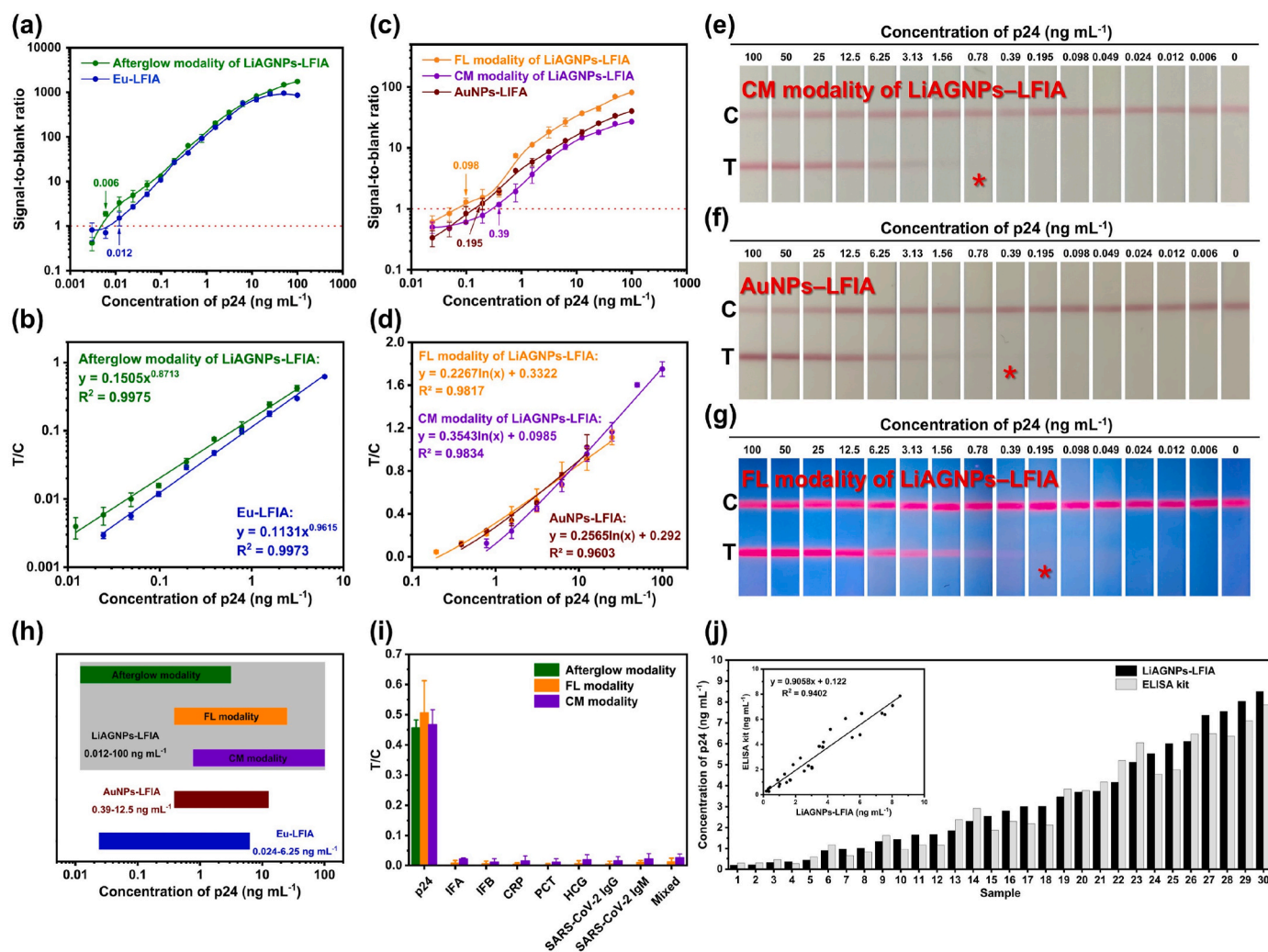
Fig. 4. Analytical evaluation of LiAGNPs–LFIA test strip for p24 antigen detection. (a) The signal-to-blank ratio for p24 antigen quantitative detection based on LiAGNPs–LFIA using afterglow signal and Eu–LFIA within the concentration range of 0–100 ng mL^{-1}. LODs were 0.006 ng mL^{-1} (afterglow modality of LiAGNPs–LFIA) and 0.012 ng mL^{-1} (Eu–LFIA), respectively. (b) The correlation curve for p24 antigen detection in human serum based on afterglow modality of LiAGNPs–LFIA and Eu–LFIA. (c) The signal-to-blank ratio for p24 antigen quantitative detection based on LiAGNPs–LFIA using FL modality and CM modality and AuNPs–LFIA within the concentration range of 0–100 ng mL^{-1}. LODs were 0.098 ng mL^{-1} (FL modality of LiAGNPs–LFIA), 0.39 ng mL^{-1} (CM modality of LiAGNPs–LFIA), and 0.195 ng mL^{-1} (AuNPs–LFIA), respectively. (d) The correlation curve for p24 antigen detection in human serum based on FL modality and CM modality of LiAGNPs–LFIA and AuNPs–LFIA. (e–g) The reacted test strip prototype photographs of LiAGNPs–LFIA (CM modality) (e) and AuNPs–LFIA (f) under room light; and under the excitation of the additional handheld flashlight (365 nm UV light) (g) in the qualitative detection of various p24 antigen concentrations ranged from 0 to 100 ng mL^{-1}. (h) The dynamic ranges of LiAGNPs–LFIA, AuNPs–LFIA, and Eu–LFIA in the assay of p24 antigen in human serum. (i) The specificity assessment of LiAGNPs–LFIA for p24 antigen in human serum by testing the signal answer intensity against other interfering proteins. (j) The results of the detected concentrations of p24 antigen between LiAGNPs–LFIA strategy and a marketable ELISA kit in testing 30 p24 antigen spiked healthy human serum samples. The inserted images are subjected to correlation analysis on the assay results gained by the two methods. The error bars were calculated from three parallel experiments.

quantitation of the proposed LiAGNPs–LFIA in FL modality and CM modality and AuNPs–LFIA were 0.098 ng mL^{-1}, 0.39 ng mL^{-1}, and 0.195 ng mL^{-1}, respectively. The excellent correlation curve between the T/C values and the concentration of p24 antigen were obtained (Fig. 4d), and the corresponding equation are as follows: y = 0.2988ln (x) + 0.2617 (R^2 = 0.9807) (FL modality of LiAGNPs–LFIA), y = 0.3543ln(x) + 0.0985 (R^2 = 0.9834) (CM modality of LiAGNPs–LFIA), and y = 0.2565ln(x) + 0.292 (R^2 = 0.9603) (AuNPs–LFIA).

For qualitative analysis of HIV-infected, the visual limit of detection (vLOD), the lowest p24 antigen concentration required to generate an apparent band at the T-line, was determined on LiAGNPs-LFIA. As revealed by the strip prototype photographs under room light, the obvious bands of LiAGNPs–LFIA (CM modality, Fig. 4e) and AuNPs–L-FIA (Fig. 4f) were readily visible to the naked eyes. The vLOD of the proposed LiAGNPs–LFIA at CM modality was found to be 0.78 ng mL^{-1}, which is only 2.0-fold higher than that obtained by AuNPs–LFIA (0.39

ng mL^{-1}) by using naked eyes. These results show that LiAGNPs–LFIA can be comparable to the mature AuNPs–LFIA using naked eyes without any instruments. Notably, under an external handheld flashlight (365 nm UV light) excitation, a more distinct band was observable on the T- and C-lines of LiAGNPs–LFIA at FL modality (Fig. 4g) with a vLOD of 0.195 ng mL^{-1}, of 4.0-fold and 2.0-fold lower than that by using CM modality and AuNPs–LFIA, respectively. The above results indicate that the CM modality of LiAGNPs provides rapid and preliminary test and if needed, the FL modality further improve the detection sensitivity, as required by specific scenarios. Fig. 4h highlights a broad dynamic range of LiAGNPs–LFIA (0.012 ng mL^{-1} – 100 ng mL^{-1}), which spans over 256-fold of AuNPs–LFIA (0.39 ng mL^{-1} – 12.5 ng mL^{-1}) and 32-fold of Eu–LFIA (0.024 ng mL^{-1} – 6.25 ng mL^{-1}). This ultrabroad dynamic range is mainly attributed to the triple detection regime, which is enabled by the inherent coloration of the LiAGNPs (for detection of 0.78–100 ng mL^{-1} p24 antigen) and their ability to generate a FL

modality under light excitation to decorate the T-line, accessing a second regime from 0.39 to 25.0 ng mL^{-1} for p24 antigen, and a particular ability to generate afterglow post LED light irradiation, accessing the third regime from 0.012 to 3.13 ng mL^{-1} for p24 antigen (Fig. 4h). The advantages of this broad triple dynamic range can be more responsive to demand scenarios for HIV diagnosis.

To assess the selectivity of LiAGNPs–LFIA test strip for p24 antigen recognition, several interfering proteins, involving influenza A protein (IFA), influenza B protein (IFB), C-reactive protein (CRP), procalcitonin (PCT), SARS-CoV-2 IgG, SARS-CoV-2 IgM, human chorionic gonadotropin (HCG), and their mixed sample were chosen as reference substances. Fig. 4i demonstrates that only a high signal answer was presented in detecting p24 antigen (3.0 ng mL^{-1}). In contrast, inappreciable signal answers were observed in detecting other proteins (1.0 µg mL^{-1}), indicating the admirable specificity of the established LiAGNPs–LFIA platform for p24 antigen assay. The accuracy and precision of LiAGNPs–LFIA were estimated by measuring the recoveries and coefficient of variation (CV) of five p24 antigen-spiked human serum samples with concentrations 3.1, 0.8, 0.2, 0.05, and 0.01 ng mL^{-1} for afterglow modality, 12.5, 6.3, 3.1, 1.6 and 0.8 ng mL^{-1} for FL modality, and 50, 25, 12.5, 6.3, and 3.1 ng mL^{-1} for CM modality, respectively. As shown in Table 1, the average recoveries of the triple signal of LiAGNPs–LFIA range from 88.5% to 116.1% with a CV of less than 12.8%, indicating an acceptable accuracy and precision for quantitative p24 antigen analysis.

Inspired by the outstanding analytical performance, the correlation between results obtained with LiAGNPs–LFIA test strips and ELISA kit for 30 p24 antigen spiked healthy human serum samples were analyzed. As shown in Fig. 4j, the results gained by the LiAGNPs–LFIA agree well with those obtained by the ELISA kit with an excellent linear correlation (y = 0.9058x + 0.122) and correlation coefficient (R^2 = 0.9402), illustrating the high reliability of LiAGNPs–LFIA for POCT of human serum samples.

3.6. LiAGNPs–LFIA for detection of IgM and IgG against SARS-CoV-2

Encouraged by the successful p24 antigen detection through the developed LiAGNPs–LFIA, the generality of this biosensor was proved by testing other biomarkers. Rapid diagnostic tools for the SARS-CoV-2 virus and antiviral antibodies are urgently needed in the COVID-19 pandemic (Chen et al., 2021; Fozouni et al., 2021; Guo et al., 2021; Lew et al., 2021). We further employed our developed LiAGNPs–LFIA strategy to realize the combined assay of SARS-CoV-2 IgM and IgG (Fig. 5a). In this immunoassay design, mouse anti-human IgM, mouse anti-human IgG, and goat anti-chicken IgY were deployed to the NC

membrane as the M-line, G-line, and C-line, respectively. In addition, two immunoprobes, LiAGNPs–SARS-CoV-2 spike protein (LiAGNPs–S antigen) and LiAGNPs–chicken IgY, were synthesized and fixed on the conjugate pad. For the COVID-19 assay, the IgM and IgG were recognized by LiAGNPs–S antigen and then settled at G-line and M-line by the mouse anti-human IgM and mouse anti-human IgG, respectively. The LiAGNPs–chicken IgY was specifically combined with goat anti-chicken IgY plugged on line C and used as a quality control output, independent of the IgM and IgG concentrations in the samples. The signal acquisition mode for IgM and IgG are the same as that for p24 antigen detection. The result explanation is shown in the Fig. 5a. The details for the characterization and optimization of the IgM and IgG testing are displayed in Figs. S16–S20. All parameter optimization processes were conducted by detecting IgM (100 ng mL^{-1}) and IgG (100 ng mL^{-1}) spiked fetal bovine serum (FBS) sample. The optimum preparation conditions of LiAGNPs–LFIA were determined by the detection signals of M-line and G-line simultaneously. Under the developed conditions, Fig. 5 b and 5c demonstrate the vLOD of LiAGNPs–LFIA strip for the assay of IgM and IgG in FBS are 31.3 and 7.8 ng mL^{-1} using CM modality and 15.6 and 3.9 ng mL^{-1} using FL modality, respectively. The quantitative LODs (the lowest target concentration corresponding to SBR >1) for IgM and IgG in FBS were found to be 0.98 and 0.24 ng mL^{-1} using afterglow signal, 15.6 and 3.9 ng mL^{-1} using FL modality, and 31.3 and 7.8 ng mL^{-1} using CM modality, respectively (Fig. 5d and e). Calibration curves between M/C or G/C value and target concentration were obtained using afterglow modality (in the range of 1.95–250 ng mL^{-1} for IgM and 0.49–31.3 ng mL^{-1} for IgG), FL modality (in the range of 31.3–500 ng mL^{-1} for IgM and 7.8–125 ng mL^{-1} for IgG), and CM modality (in the range of 62.5–1000 ng mL^{-1} for IgM and 7.8–125 ng mL^{-1} for IgG), respectively (Fig. S21, inset). These results illustrate that our proposed LiAGNPs can serve as a promising immunolabel on the LFIA platform for reliable POCT of infectious disease under different application scenarios.

4. Conclusion

In conclusion, we proposed a novel light-initiated afterglow nano-reporter, that is, LiAGNPs, and demonstrate its application for infectious disease detection on the LFIA platform. The synergy between the two employed block elements in LiAGNPs promotes cyclic production of $^1O_2$, resulting in an enhanced afterglow intensity and a prolonged afterglow emission. Thanks to the cyclic triggering chemical events, the afterglow emission of LiAGNPs decay mildly, favoring time-resolved signal collection for sensitive detection. Experimental detection results show higher sensitivity of LiAGNPs at afterglow modality compared to Eu-chelate-based time-resolved LFIA in the p24 antigen detection. Importantly, the detection sensitivity of LiAGNPs–LFIA might be further enhanced by prolonging the light initiation time and the afterglow signal collection time of the analyzer. Besides, the intrinsic color and FL properties of TTMN dye endow LiAGNPs with colorimetric and fluorescent signal outputs, providing applications in different demanding scenarios. The generality of LiAGNPs–LFIA was testified by detecting SARS-CoV-2 specific IgM and IgG. Collectively, the tri-optical behavior of LiAGNPs particularly with outstanding afterglow performance, not only enhance the analytical sensitivity of LFIA, but also provide a versatile LFIA platform for different requirements in disease diagnostics.

CRediT authorship contribution statement

Liangwen Hao: Conceived the project and designed the experiments, Formal analysis, and, Data curation, and, Writing – original draft. **Weitao Yang:** Conceived the project and designed the experiments, Formal analysis, and, Data curation, and, Writing – original draft. **Yan Xu:** Conceived the project and designed the experiments, Formal analysis, and, Data curation, and, Writing – original draft. **Tianming Cui:** Formal analysis, and, Data curation. **Guoqi Zhu:** Formal analysis, and, Data curation. **Weiwei Zeng:** Formal analysis, and, Data curation.
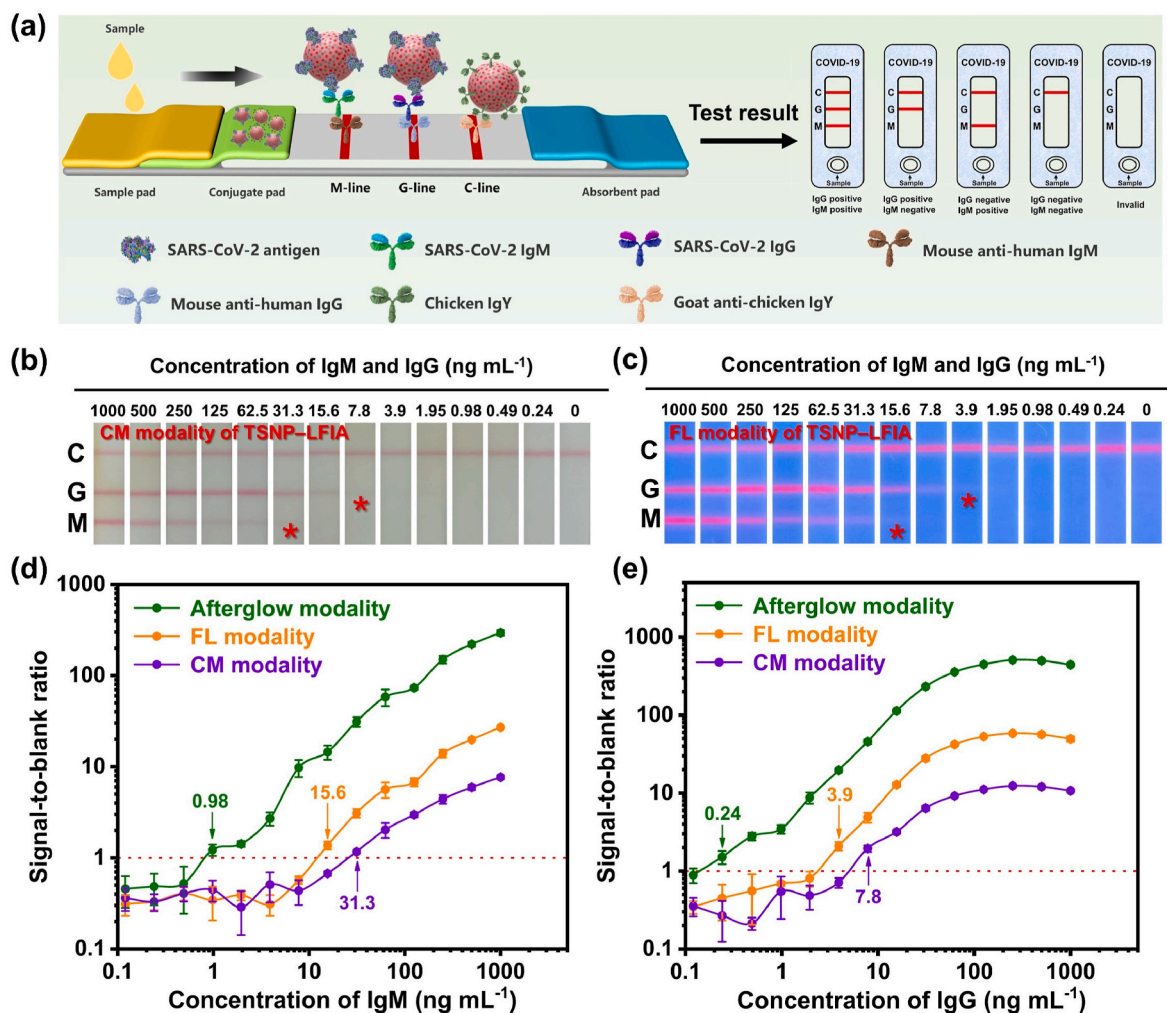
Table 1
Average recovery and CV for the assay of p24 antigen in human serum (n = 5) using LiAGNPs–LFIA test strips.

Detection modality of LiAGNPs–LFIA	Added p24 antigen (ng mL^{-1})	Detected p24 antigen (ng mL^{-1})	Recovery (%)	CV (%)
Afterglow	3.1	3.1 ± 0.4	101.8	12.2
	0.8	0.7 ± 0.06	112.4	7.9
	0.2	0.2 ± 0.01	97.6	4.6
	0.05	0.05 ± 0.004	108.0	9.0
	0.01	0.01 ± 0.002	94.0	11.7
FL	12.5	11.8 ± 1.1	106.4	9.4
	6.3	6.8 ± 0.6	93.1	8.5
	3.1	2.8 ± 0.3	114.2	11.4
	1.6	1.5 ± 0.2	107.4	12.8
	0.8	0.7 ± 0.05	116.1	7.1
CM	50.0	57.0 ± 5.2	88.5	9.2
	25.0	21.8 ± 1.1	105.0	5.0
	12.5	13.0 ± 1.3	97.2	10.3
	6.3	6.0 ± 0.3	106.6	5.8
	3.1	3.0 ± 0.2	105.1	7.0

Fig. 5. Analytical evaluation of LiAGNPs–LFIA test strip for SARS-Cov-2 IgM and IgG in fetal bovine serum. (a) Schematic representation and interpretation of detection results for SARS-Cov-2 IgM and IgG using LiAGNPs–LFIA test strip platform. The rise of signal bands on M-, G-, and C-line were positive for SARS-Cov-2 IgM and IgG; The presence of signal bands on M- and C-line indicate SARS-Cov-2 IgM positivity; The appearance of signal bands on G- and C-line reveal positive IgG; Only the signal band appears on the C-line, indicating that COVID-19 is negative; The absence of signal bands on the M-, G-, and C-line indicate an invalid test result. (b–c) The reacted test strip prototype photographs of LiAGNPs–LFIA using CM modality under room light (b) and using the FL modality under the excitation of the additional handheld flashlight (365 nm UV light) (c) in the qualitative detection of various SARS-Cov-2 IgM and IgG concentrations over the range of 0–1000 ng mL^{-1}. (d) The signal-to-blank ratio for quantitative detection of SARS-Cov-2 IgM by LiAGNPs-LFIA over the range of 0–1000 ng mL^{-1}. LODs were 0.98 ng mL^{-1} (afterglow modality), 15.6 ng mL^{-1} (FL modality), and 31.3 ng mL^{-1} (CM modality), respectively. (e) The signal-to-blank ratio for IgG quantitative detection based on LiAGNPs–LFIA within the concentration range of 0–1000 ng mL^{-1}. LODs were 0.24 ng mL^{-1} (afterglow modality), 3.9 ng mL^{-1} (FL modality), and 7.8 ng mL^{-1} (CM modality), respectively. The error bars were calculated from three parallel experiments.

Kexin Bian: Formal analysis, and, Data curation. **Hongying Liang:** Formal analysis, and, Data curation, and. **Pengfei Zhang:** Formal analysis, and, Data curation. **Bingbo Zhang:** Conceptualization, Methodology, reviewing & editing paper, instruction, and revision.

Declaration of competing interest

The authors declare that they have no known competing financial interests or personal relationships that could have appeared to influence the work reported in this paper.

Acknowledgment

Appendix A. Supplementary data

Supplementary data to this article can be found online at https://doi.org/10.1016/j.bios.2022.114411.

References

Ackerman, C.M., Myhrvold, C., Thakku, S.G., Freije, C.A., Metsky, H.C., Yang, D.K., Ye, S.H., Boehm, C.K., Kosoko-Thoroddsen, T.F., Kehe, J., Nguyen, T.G., Carter, A., Kulesa, A., Barnes, J.R., Dugan, V.G., Hung, D.T., Blainey, P.C., Sabeti, P.C., 2020. Nature 582 (7811), 277–282.

Baker, R.E., Mahmud, A.S., Miller, I.F., Rajeev, M., Rasambainarivo, F., Rice, B.L., Takahashi, S., Tatem, A.J., Wagner, C.E., Wang, L.F., Wesolowski, A., Metcalf, C.J.E., 2021. Nat. Rev. Microbiol. 20, 193–205.

Brendish, N.J., Poole, S., Naidu, V.V., Mansbridge, C.T., Norton, N.J., Wheeler, H., Presland, L., Kidd, S., Cortes, N.J., Borca, F., Phan, H., Babbage, G., Visseaux, B., Ewings, S., Clark, T.W., 2020. Lancet Respir. Med. 8 (12), 1192–1200.

Chen, J., Hao, L., Hu, J., Zhu, K., Li, Y., Xiong, S., Huang, X., Xiong, Y., Tang, B.Z., 2022. Angew. Chem., Int. Ed. 61 (7), e202112031.

Chen, R., Ren, C., Liu, M., Ge, X., Qu, M., Zhou, X., Liang, M., Liu, Y., Li, F., 2021. ACS Nano 15 (5), 8996–9004.

Chen, X., Leng, Y., Hao, L., Duan, H., Yuan, J., Zhang, W., Huang, X., Xiong, Y., 2020. Theranostics 10 (8), 3737–3748.

Elledge, S.K., Zhou, X.X., Byrnes, J.R., Martinko, A.J., Lui, I., Pance, K., Lim, S.A., Glasgow, J.E., Glasgow, A.A., Turcios, K., Iyer, N.S., Torres, L., Peluso, M.J., Henrich, T.J., Wang, T.T., Tato, C.M., Leung, K.K., Greenhouse, B., Wells, J.A., 2021. Nat. Biotechnol. 39 (8), 928–935.

Ferreira, A.L., de Lima, L.F., Torres, M.T., de Araujo, W.R., de la Fuente-Nunez, C., 2021. ACS Nano 15 (11), 17453–17462.

Fozouni, P., Son, S., Diaz de Leon Derby, M., Knott, G.J., Gray, C.N., D'Ambrosio, M.V., Zhao, C., Switz, N.A., Kumar, G.R., Stephens, S.I., Boehm, D., Tsou, C.L., Shu, J., Bhuiya, A., Armstrong, M., Harris, A.R., Chen, P.Y., Osterloh, J.M., Meyer-Franke, A., Joehnk, B., Walcott, K., Sil, A., Langelier, C., Pollard, K.S., Crawford, E. D., Puschnik, A.S., Phelps, M., Kistler, A., DeRisi, J.L., Doudna, J.A., Fletcher, D.A., Ott, M., 2021. Cell 184 (2), 323–333 e329.

Ganguli, A., Mostafa, A., Berger, J., Aydin, M.Y., Sun, F., Ramirez, S.A.S., Valera, E., Cunningham, B.T., King, W.P., Bashir, R., 2020. Proc. Natl. Acad. Sci. U. S. A 117 (37), 22727–22735.

Gray, E.R., Bain, R., Varsaneux, O., Peeling, R.W., Stevens, M.M., McKendry, R.A., 2018. AIDS 32 (15), 2089–2102.

Grzelak, L., Temmam, S., Planchais, C., Demeret, C., Tondeur, L., Huon, C., Guivel-Benhassine, F., Staropoli, I., Chazal, M., Dufloo, J.J.S.t.m., 2020. Sci. Transl. Med. 12 (559), eabc3103.

Guo, H., Song, X., Lei, W., He, C., You, W., Lin, Q., Zhou, S., Chen, X., Chen, Z., 2019. Angew. Chem., Int. Ed. 58 (35), 12195–12199.

Guo, K., Wustoni, S., Koklu, A., Diaz-Galicia, E., Moser, M., Hama, A., Alqahtani, A.A., Ahmad, A.N., Alhamlan, F.S., Shuaib, M., Pain, A., McCulloch, I., Arold, S.T., Grunberg, R., Inal, S., 2021. Nat. Biomed. Eng. 5 (7), 666–677.

Hao, L., Leng, Y., Zeng, L., Chen, X., Chen, J., Duan, H., Huang, X., Xiong, Y., Chen, X., 2020. Adv. Sci. 7 (2), 1902433.

Hu, J., Jiang, Y.Z., Wu, L.L., Wu, Z., Bi, Y., Wong, G., Qiu, X., Chen, J., Pang, D.W., Zhang, Z.L., 2017a. Anal. Chem. 89 (24), 13105–13111.

Hu, L.M., Luo, K., Xia, J., Xu, G.M., Wu, C.H., Han, J.J., Zhang, G.G., Liu, M., Lai, W.H., 2017b. Biosens. Bioelectron. 91, 95–103.

Huang, L., Jin, J., Ao, L., Jiang, C., Zhang, Y., Wen, H.M., Wang, J., Wang, H., Hu, J., 2020. ACS Appl. Mater. Interfaces 12 (52), 58149–58160.

Huang, X., Zhou, Y., Ding, L., Yu, G., Leng, Y., Lai, W., Xiong, Y., Chen, X., 2019. Small 15 (51), e1903861.

Ji, T., Xu, X., Wang, X., Cao, N., Han, X., Wang, M., Chen, B., Lin, Z., Jia, H., Deng, M., Xia, Y., Guo, X., Lei, M., Liu, Z., Zhou, Q., Chen, G., 2020. ACS Nano 14 (12), 16864–16874.

Jiang, Y., Huang, J., Zhen, X., Zeng, Z., Li, J., Xie, C., Miao, Q., Chen, J., Chen, P., Pu, K., 2019. Nat. Commun. 10 (1), 2064.

Karim, N., Afroj, S., Lloyd, K., Oaten, L.C., Andreeva, D.V., Carr, C., Farmery, A.D., Kim, I.D., Novoselov, K.S., 2020. ACS Nano 14 (10), 12313–12340.

Kirtane, A.R., Verma, M., Karandikar, P., Furin, J., Langer, R., Traverso, G., 2021. Nat. Nanotechnol. 16 (4), 369–384.

Kyme, H., Lee, C.T., Kim, Y.T., Lee, J.H., 2019. Talanta 192, pp. 189–196.

Lee, K.W., Kim, K.R., Chun, H.J., Jeong, K.Y., Hong, D.K., Lee, K.N., Yoon, H.C., 2020. Biosens. Bioelectron. 163, 112284.

Lew, T.T.S., Aung, K.M.M., Ow, S.Y., Amrun, S.N., Sutarlie, L., Ng, L.F.P., Su, X., 2021. ACS Nano 15 (7), 12286–12297.

Li, J., Duan, H., Xu, P., Huang, X., Xiong, Y., 2016. RSC Adv. 6 (31), 26178–26185.

Li, J., Lin, R., Yang, Y., Zhao, R., Song, S., Zhou, Y., Shi, J., Wang, L., Song, H., Hao, R., 2021. ACS Appl. Mater. Interfaces 13 (19), 22262–22270.

Liu, D., Ju, C., Han, C., Shi, R., Chen, X., Duan, D., Yan, J., Yan, X., 2020a. Biosens. Bioelectron. 173, 112817.

Liu, Q., Cheng, S., Chen, R., Ke, J., Liu, Y., Li, Y., Feng, W., Li, F., 2020b. ACS Appl. Mater. Interfaces 12 (4), 4358–4365.

Liu, Y., Zhan, L., Qin, Z., Sackrison, J., Bischof, J.C., 2021. ACS Nano 15 (3), 3593–3611.

Lucky, S.S., Soo, K.C., Zhang, Y., 2015. Chem. Rev. 115 (4), 1990–2042.

Ma, Q., Wang, J., Li, Z., Lv, X., Liang, L., Yuan, Q., 2019. Small 15 (32), e1804969.

Miller, B.S., Bezinge, L., Gliddon, H.D., Huang, D., Dold, G., Gray, E.R., Heaney, J., Dobson, P.J., Nastouli, E., Morton, J.J.L., McKendry, R.A., 2020. Nature 587 (7835), 588–593.

Norman, M., Gilboa, T., Ogata, A.F., Maley, A.M., Cohen, L., Busch, E.L., Lazarovits, R., Mao, C.P., Cai, Y., Zhang, J., Feldman, J.E., Hauser, B.M., Caradonna, T.M., Chen, B., Schmidt, A.G., Alter, G., Charles, R.C., Ryan, E.T., Walt, D.R., 2020. Nat. Biomed. Eng. 4 (12), 1180–1187.

Oeschger, T.M., McCloskey, D.S., Buchmann, R.M., Choubal, A.M., Boza, J.M., Mehta, S., Erickson, D., 2021. Acc. Chem. Res. 54 (19), 3656–3666.

Pandori, M.W., Hackett Jr., J., Louie, B., Vallari, A., Dowling, T., Liska, S., Klausner, J.D., 2009. J. Clin. Microbiol. 47 (8), 2639–2642.

Parolo, C., Sena-Torralba, A., Bergua, J.F., Calucho, E., Fuentes-Chust, C., Hu, L., Rivas, L., Alvarez-Diduk, R., Nguyen, E.P., Cinti, S., Quesada-Gonzalez, D., Merkoci, A., 2020. Nat. Protoc. 15 (12), 3788–3816.

Paterson, A.S., Raja, B., Garvey, G., Kolhatkar, A., Hagström, A.E.V., Kourentzi, K., Lee, T.R., Willson, R.C., 2014. Anal. Chem. 86 (19), 9481–9488.

Qi, L., Yang, M., Chang, D., Zhao, W., Zhang, S., Du, Y., Li, Y., 2021. Angew. Chem., Int. Ed. 60 (47), 24823–24827.

Qin, Z., Chan, W.C., Boulware, D.R., Akkin, T., Butler, E.K., Bischof, J.C., 2012. Angew. Chem., Int. Ed. 51 (18), 4358–4361.

Santiago, G.A., Vazquez, J., Courtney, S., Matias, K.Y., Andersen, L.E., Colon, C., Butler, A.E., Roulo, R., Bowzard, J., Villanueva, J.M., Munoz-Jordan, J.L., 2018. Nat. Commun. 9 (1), 1391.

Sebba, D., Lastovich, A.G., Kuroda, M., Fallows, E., Johnson, J., Ahouidi, A., Honko, A. N., Fu, H., Nielson, R., Carruthers, E.J.S.t.m., 2018. Sci. Transl. Med. 10 (471), eaat0944.

Shah, K.G., Yager, P., 2017. Anal. Chem. 89 (22), 12023–12029.

Shi, X., Sung, S.H.P., Chau, J.H.C., Li, Y., Liu, Z., Kwok, R.T.K., Liu, J., Xiao, P., Zhang, J., 2020. Small Methods 4 (7), 2000046.

Sun, G., Xie, Y., Sun, L., Zhang, H., 2021. Nanoscale Horiz 6 (10), 766–780.

Wang, D., He, S., Wang, X., Yan, Y., Liu, J., Wu, S., Liu, S., Lei, Y., Chen, M., Li, L., Zhang, J., Zhang, L., Hu, X., Zheng, X., Bai, J., Zhang, Y., Zhang, Y., Song, M., Tang, Y., 2020. Nat. Biomed. Eng. 4 (12), 1150–1158.

Wang, C., Liu, M., Wang, Z., Li, S., Deng, Y., He, N., 2021a. Nano Today 37, 101092.

Wang, J., Jiang, C., Jin, J., Huang, L., Yu, W., Su, B., Hu, J., 2021b. Angew. Chem., Int. Ed. 60 (23), 13042–13049.

Wang, D., Su, H., Kwok, R.T.K., Shan, G., Leung, A.C.S., Lee, M.M.S., Sung, H.H.Y., Williams, I.D., Lam, J.W.Y., Tang, B.Z., 2017. Adv. Funct. Mater. 27 (46), 1704039.

Wang, J., Li, J.L., Yu, J.N., Zhang, H.W., Zhang, B.B., 2018. ACS Nano 12 (5), 4246–4258.

Woo, C.H., Jang, S., Shin, G., Jung, G.Y., Lee, J.W., 2020. Nat. Biomed. Eng. 4 (12), 1168–1179.

Yao, Z., Drecun, L., Aboualizadeh, F., Kim, S.J., Li, Z., Wood, H., Valcourt, E.J., Manguiat, K., Plenderleith, S., Yip, L., Li, X., Zhong, Z., Yue, F.Y., Closas, T., Snider, J., Tomic, J., Drews, S.J., Drebot, M.A., McGeer, A., Ostrowski, M., Mubareka, S., Rini, J.M., Owen, S., Stagljar, I., 2021. Nat. Commun. 12 (1), 1806.

Yousefi, H., Mahmud, A., Chang, D., Das, J., Gomis, S., Chen, J.B., Wang, H., Been, T., Yip, L., Coomes, E., Li, Z., Mubareka, S., McGeer, A., Christie, N., Gray-Owen, S., Cochrane, A., Rini, J.M., Sargent, E.H., Kelley, S.O., 2021. J. Am. Chem. Soc. 143 (4), 1722–1727.

Zhang, Y., Wang, L.L., Wang, W.L., Yang, C., Feng, Y.W., Shi, X.L., 2021a. Talanta 232, 122427.

Zhang, Z., Xu, W., Xiao, P., Kang, M., Yan, D., Wen, H., Song, N., Wang, D., Tang, B.Z., 2021b. ACS Nano 15 (6), 10689–10699.

Zhang, G.G., Xu, S.L., Xiong, Y.H., Duan, H., Chen, W.Y., Li, X.M., Yuan, M.F., Lai, W.H., 2019. Biosens. Bioelectron. 135, 173–180.